



# Underwater image dehazing and denoising via curvature variation regularization

Guojia Hou<sup>1,2</sup>  · Jingming Li<sup>1</sup> · Guodong Wang<sup>1</sup> · Zhenkuan Pan<sup>1</sup> · Xin Zhao<sup>1</sup>

Received: 9 April 2019 / Revised: 7 December 2019 / Accepted: 17 February 2020

Published online: 15 April 2020

© Springer Science+Business Media, LLC, part of Springer Nature 2020

## Abstract

Challenges for underwater captured image processing often lie in images degraded with haze, noise and low contrast, caused by absorption and scattering of the light during propagation. In this paper, we aim to establish a novel total variation and curvature based approach that can properly deal with these problems to achieve dehazing and denoising simultaneously. Integration with the underwater image formation model is successfully realized by formulating the global background light and the transmission map derived from the improved dark channel prior and underwater red channel prior into our variational framework respectively. Moreover, the generated non-smooth optimization problem is solved by the alternating direction method of multipliers (ADMM). Extensive experiments including real underwater image application tests and convergence curves display the significant gains of the proposed variational curvature model and developed ADMM algorithm. Qualitative and quantitative comparisons with several state-of-the-art methods as well as four evaluation metrics are further conducted to quantify the improvements of our fusion approach.

**Keywords** Underwater image · Dehazing and denoising · Image formation model · Curvature variation · ADMM

## 1 Introduction

In underwater image acquisition process [35], some quality problems generally occur in captured images, which are derived from many factors. For example, the light direction inevitably varies because scattering always exists. Likewise, the light energy level can not

---

✉ Guojia Hou  
hgjouc@126.com

<sup>1</sup> College of Computer Science & Technology, Qingdao University, No. 308 Ningxia Road, Qingdao, China

<sup>2</sup> School of Automation, Qingdao University, No. 308 Ningxia Road, Qingdao, China

keep on an even keel due to a portion of light is absorbed by objects. In addition, the maximum attenuation of red light in the underwater environment always results in color distortion [1]. Degraded underwater images have many limitations for oceanographic survey, ocean environments exploitation, and underwater objection detection [24, 33]. Therefore, underwater image processing is full of challenging owing to the specific physical characteristics of underwater environment. It is hence essential to develop an effective technology which allows for efficient and robust restoration for underwater images.

Many attempts to automate underwater image enhancement and restoration were proposed in recent decades. Some traditional image enhancement algorithms, such as histogram equalization [17] and probability-based method [10] can efficiently improve visual quality. However, these methods are not relying on the underwater image formation model (IFM) and the principle of underwater image quality degradation. Thus, the restored results can not meet our special demands under different challenge scenes. Among most of the IFM based algorithms, the dark channel prior (DCP) proposed by He et al. [16] was originally applied to estimate the transmission map and global background light. Afterward, various researches for underwater image dehazing [15, 4, 20, 29, 26] derived from DCP were published. Unfortunately, the traditional DCP is not completely suitable for underwater environment due to the maximum attenuation of red light. In [16], He et al. used the dark channel to obtain the air light, and selected the top 0.1% pixels with the largest brightness in the dark channel. However, the global background light of underwater image was easily interfered by white objects in water, which made the background light value estimated too high. To address this problem, Wen et al. [44] introduced an underwater dark channel prior (UDCP), which only need the information from blue and green channels. While DCP and UDCP could increase the effect of green and blue and deepen the background. Galdran et al. [11] inverted red channel and proposed a red channel method to recover color associated to short wavelengths. However, the Galdran's method based algorithms didn't pay attention to denoising task and even increased the noise level in results. This led to different levels of noise remained in the restored results, which made it more difficult for image analysis.

It is well known that the estimations of transmission map and global background light play crucial roles in obtaining a haze-free underwater image. Carlevaris-Bianco et al. [2] proposed a simple and effective maximum intensity prior (MIP) to remove the effects of light scattering. They estimated the depth scene by exploiting maximum intensity in attenuation between the three RGB channels. Peng et al. [32] employed image blurriness and light absorption to improve its accuracy in estimating the transmission map and background light. All these method could recover images with good performance validated by objective evaluations, but without any consideration about the texture and edge information of the image. Moreover, most underwater restoration methods only focused on how to improve the estimation of transmission map and background light, while ignored the influence of noise appeared in the underwater image, resulting in noise amplification and valuable information loss. Therefore, techniques in terms of underwater image dehazing and denoising should be an important tool in underwater applications.

Recently, variational methods based on partial differential equations and differential geometry have been widely and excellently applied in image processing, especially in image denoising [45, 3, 47, 43], dehazing [12, 42, 8, 19], segmentation [39, 41, 7, 28], and inpainting [48, 6]. The initial variational model was proposed by Tikhonov [40] for noise reduction, which was composed of data term and regularization term. The Data term indicated the relationship between denoising image and original image, and the regularization term can

control the smoothness on the restored image by introducing the first or second derivative. In 1992, Osher et al. [34] improved the Tikhonov model by employing total variation (TV) term as the regularizer that can produce excellent edge preservation results. In [23], Kimmel et al. proposed a variational Retinex framework motivated by Retinex theory. The proposed formulation unified the previous different Retinex methods. Fang et al. [8] proposed a new fast variational approach for atmospheric images dehazing and denoising. They utilized the window adaptive algorithm to estimate the transmission map and further employed multiple-splitting Chambolle-Pock algorithm without inner loop to boost its efficiency. The TV regularizer approximated the piecewise constant function with a good performance in noise suppression, but the problem of ‘staircase effect’ existed in image region. To resolve this limitation, Shu et al. [36] presented a high-order total generalized variation-regularized variational (TGV) model. Although TGV alleviates the weakness of TV, it may blur the details of the inflection point. Hou et al. [18] solved the problem of non-uniform illumination utilizing the nonlocal differential operator, their proposed  $L^1$ -based nonlocal total variational (NLTVL<sup>1</sup>) model was derived from variational framework for Retinex. In [38, 37, 49], the curvature regularizer was successfully used to maintain the inflection point feature. The current variational restoration methods are all based on the propagation process of light in the atmosphere.

Motivated by total variational methods [42, 8] for dehazing fog-degraded image, we propose a novel variational approach with total curvature and total variation based on underwater image formation model. The main contributions of the proposed method include:

- (i) We successfully incorporate the underwater image formation model into variational image restoration framework;
- (ii) The data term and the regularization term of the unified variational model are designed deriving from variational Retinex model;
- (iii) The alternating direction method of multipliers (ADMM) is further intentionally designed for the main challenge of the non-smooth problem and computation efficiency.

The rest of our work is organized as follows. The underwater optical image formation model is briefly introduced in Section 2. Section 3 describes the proposed model and its numerical solution of ADMM algorithm. The qualitative and quantitative evaluation results are given in Section 4. Concluding remarks are presented in Section 5.

## 2 Underwater optical image formation model

The proposed method is based on the simplified underwater optical image formation model [30, 21], which is given as

$$I(x, y) = J(x, y) \cdot t(x, y) + B \cdot (1 - t(x, y)) \quad (1)$$

where  $I(x, y)$  represents the observed underwater image,  $J(x, y)$  is the recovered image,  $t(x, y)$  is the underwater transmission map, and  $B$  denotes the underwater global background light. Given a known underwater image  $I(x, y)$ , we need to obtain the information about the underwater transmission map (UTM) and underwater global background light (UGBL) to restore the latent image.

Empirically, the value of underwater global background light  $B$  is usually replaced with the brightest pixel in the image  $I(x, y)$ . However, in most cases, the brightest pixel in foreground will be mistaken as the UGBL. In [25], Li et al. employed a hierarchical searching technique based on quad-tree subdivision [22] to estimate the UGBL. Unfortunately, in fact the estimated UGBL is not the exact brightest pixel in the image since some pixels with smaller intensity values will be included in the candidate area. In order to tackle this problem, we first pick top 0.1% brightest pixels in each dark channel as the candidate pixels, next the value with the largest difference between red and blue dark channels are selected as the underwater global background light, which ensures its robustness and accuracy. That's because the energy of red light is absorbed largely, followed by the green and blue light.

After the UGBL is determined, the recovered underwater image subsequently depends on the estimation of underwater transmission map. In most cases, although DCP method is the most popular and effective method to estimate UTM, it is not suitable for underwater scene. Fortunately, a novel underwater dark channel prior (UDCP) is specially designed for underwater image dehazing. The definition of UDCP is expressed as

$$J^{udark}(x) = \min_{y \in \Omega(x)} \left( \min_{c \in \{G, B\}} (J^c(y)) \right) \quad (2)$$

where  $\Omega(x)$  refers to a window centered on the pixel  $x$ ,  $c$  represents the color channels  $c \in \{G, B\}$ .

Practically, red color associated to shortest wavelength have the fastest attenuation rate. In our work, we employ a red channel technique [11] to first estimate the UTM of red channel, the expression is as follow.

$$t(x)^R = 1 - \omega \min_{y \in \Omega(x)} \left( \min \frac{I_R}{B_R} \right) \quad (3)$$

where  $R$  denotes the red channel,  $\omega$  is a constant ( $0 < \omega \leq 1$ ) controlling the level of the dehazing. Then we can obtain the UTMs of green and blue channels. The light is set to be uniform based on the Lambert-Beer law [13], the underwater transmission map  $t$  is rewritten as

$$t_\lambda(x) = e^{(-\beta^\lambda d(x))} \quad (4)$$

where  $\beta^\lambda$  is the attenuation coefficient of different channel,  $d(x)$  is the depth distance.

According to [14], the linear relationship between attenuation coefficient and wavelengths of light can be expressed as

$$\begin{cases} \frac{\beta^G}{\beta^R} = \frac{\beta^R(-0.00113\lambda^G + 1.62517)}{B^G(-0.00113\lambda^R + 1.62517)} \\ \frac{\beta^B}{\beta^R} = \frac{\beta^R(-0.00113\lambda^G + 1.62517)}{B^G(-0.00113\lambda^R + 1.62517)} \end{cases} \quad (5)$$

where  $\frac{\beta^G}{\beta^R}$  and  $\frac{\beta^B}{\beta^R}$  represent the G-R and B-R attenuation coefficient ratios, respectively. In general, the values of  $\beta_R$ ,  $\beta_G$  and  $\beta_B$  are empirically selected with 620 nm, 540 nm, and 450 nm, respectively. Combining with Eq. (4) and Eq. (5), we can obtain that

$$\begin{cases} t^G(x) = t^R(x)^{\frac{\beta^G}{\beta^R}} \\ t^B(x) = t^R(x)^{\frac{\beta^B}{\beta^R}} \end{cases} \quad (6)$$

### 3 A new formulation with developed ADMM algorithm

A novel variational model with curvature regularization integrated with the underwater image formation model will be described in this section. This section starts with how we achieve this novel model under classic variational framework by reformulating variables based on underwater optical image formation model, followed by implementation procedure of the ADMM algorithm.

Obviously, Eq. (1) can be easily rearranged as

$$(B - J(x, y)) = \frac{1}{t(x, y)} \cdot (B - I(x, y)) \quad (7)$$

In order to change product form into add form, Eq. (7) can be converted to

$$\log(B - J(x, y)) = \log \frac{1}{t(x, y)} + \log(B - I(x, y)) \quad (8)$$

For clarity, we set  $s = \log(B - J(x, y))$ ,  $r = \log\left(\frac{1}{t(x, y)}\right)$ ,  $l = \log(B - I(x, y))$ , then Eq. (8) can be rewritten as

$$s = r + l \quad (9)$$

In [42, 8], the variational model has been successfully combined with the foggy image formation model, inspired by them, we minimize the following energy functional to recover the image  $s$ .

$$E(r, s) = \alpha \int_{\Omega} |\nabla \cdot \frac{\nabla r}{|\nabla r|}| dx + \beta \int_{\Omega} |\nabla s| dx + \frac{1}{2} \int_{\Omega} |s - l - r|^2 dx + \frac{\lambda}{2} \int_{\Omega} |r - r_0|^2 dx \quad (10)$$

where curvature item  $\nabla \cdot \frac{\nabla r}{|\nabla r|}$  and TV item  $|\nabla s|$  are the regularization items, which keep the details of underwater recovered image while removing noise,  $|r - r_0|$  control the similarity of  $r$  and initial  $r_0$ . The data term  $|s - l - r|^2$  maintains the fidelity between the restored image and original degraded image.  $\alpha, \beta, \lambda$  are positive parameters wherein  $\alpha$  and  $\beta$  determine the degree of denoising, their values are empirically selected with  $\alpha, \beta \in [1 - 10]$ ,  $\lambda$  plays a binding role on  $r$  and the larger values indicate more important on the corresponding items, its value is application-based. After testing experiment, the value of  $\lambda \in [0.8 - 1.5]$  can satisfy the various underwater challenge scenes.  $r_0 = \log\left(\frac{1}{t_0}\right)$  represents the initial value of  $r$ .

The problem of Eq. (10) is mathematically ill-posed, which can be resolved by using the ADMM algorithm. Its implementation for the proposed variational model is given below.

First, we introduce the auxiliary variables  $\vec{p} = \nabla r, \vec{n} = \frac{\vec{p}}{|\vec{p}|}, q = \nabla \vec{n}, \vec{w} = \nabla s, \vec{m} \approx \vec{n}$ .

Based on this observation, Eq. (10) can be transformed into the following iterative optimization form:

$$\begin{aligned}
 & (r, s, \vec{p}, q, \vec{n}, \vec{m}, \vec{w}) \\
 & = \operatorname{argmin} \left\{ \begin{aligned} & \alpha \int_{\Omega} |q| dx + \frac{1}{2} \int_{\Omega} |s-l-r|^2 dx + \int_{\Omega} \sigma_1^k (|\vec{p}-\vec{p} \cdot \vec{m}|) dx \\ & + \frac{\mu_1}{2} \int_{\Omega} (\vec{p}-\vec{p} \cdot \vec{m})^2 dx + \int_{\Omega} \vec{\sigma}_2^k (\vec{p}-\nabla r) dx + \frac{\mu_2}{2} \int_{\Omega} (\vec{p}-\nabla r)^2 dx \\ & + \int_{\Omega} \sigma_3^k (q-\nabla \vec{n}) dx + \frac{\mu_3}{2} \int_{\Omega} (q-\nabla \vec{n})^2 dx + \int_{\Omega} \vec{\sigma}_4^k (\vec{n}-\vec{m}) dx \\ & + \frac{\mu_4}{2} \int_{\Omega} (\vec{n}-\vec{m})^2 dx + \beta \int_{\Omega} |\vec{w}| dx + \int_{\Omega} \vec{\sigma}_5^k (\vec{w}-\nabla s) dx \\ & + \frac{\mu_5}{2} \int_{\Omega} (\vec{w}-\nabla s)^2 dx + \frac{\lambda}{2} \int_{\Omega} (r-r_0)^2 dx \end{aligned} \right\} \quad (11)
 \end{aligned}$$

where  $\sigma_1, \vec{\sigma}_2, \sigma_3, \vec{\sigma}_4, \vec{\sigma}_5$  are the Lagrange multipliers, and  $\mu_1, \mu_2, \mu_3, \mu_4, \mu_5$  are positive parameters to compensate for the five Lagrange items.  $k$  represents the step number of iterations.

Then the minimization problem (11) can be decomposed into eight subproblems and each sub-problem of minimization is carried out with respect to one variable while keeping other variables constant temporarily. Their detailed solving procedures are given step-by-step as follows.

*Step 1:* fix  $s, q, \vec{p}, \vec{n}, \vec{m}, \vec{w}$  to solve  $r$

$$\varepsilon_1(r) = \min \left\{ \begin{aligned} & E(r) = \frac{1}{2} \int_{\Omega} (s-l-r)^2 dx + \int_{\Omega} \vec{\sigma}_2^k (\vec{p}-\nabla r) dx \\ & + \frac{\mu_2}{2} \int_{\Omega} (\vec{p}-\nabla r)^2 dx + \frac{\lambda}{2} \int_{\Omega} |r-r_0|^2 dx \end{aligned} \right\} \quad (12)$$

The Euler-Lagrange (E-L) equation of Eq. (12) is

$$r + l - s + \nabla \vec{\sigma}_2 + \mu_2 \nabla (\vec{p} - \nabla r) + \lambda (r - r_0) = 0 \quad (13)$$

The final  $r$  can be obtained using Jacobi iteration method:

$$r_{i,j}^{k+1} = \frac{s^k - l^k - \nabla \vec{\sigma}_2^k - \mu_2 \nabla \vec{p}^k + \mu_2 R^k + \lambda r_0}{1 + 4\mu_2 + \lambda} \quad (14)$$

where  $R = r_{i+1,j}^k + r_{i-1,j}^k + r_{i,j+1}^k + r_{i,j-1}^k - 4r_{i,j}^k$

*Step 2:* fix  $r, \vec{p}, q, \vec{n}, \vec{m}, \vec{w}$  to solve  $s$ :

$$\varepsilon_2(s) = \min \left\{ \begin{aligned} & E(s) = \frac{1}{2} \int_{\Omega} (s-l-r)^2 dx + \int_{\Omega} \vec{\sigma}_5^k (\vec{w}-\nabla s) dx + \frac{\mu_5}{2} \int_{\Omega} (\vec{w}-\nabla s)^2 dx \end{aligned} \right\} \quad (15)$$

Its Euler-Lagrange (E-L) equation is

$$s-l-r+\nabla\vec{\sigma}_5+\mu_5\nabla\vec{w}-\mu_5\Delta s=0 \quad (16)$$

Then

$$s^{k+1}=\frac{\mu_5 S+r+l-\nabla\vec{\sigma}_5^k-\mu_5\nabla\vec{w}}{1+4\mu_5} \quad (17)$$

where  $S=s_{l+1,j}^k+s_{l-1,j}^k+s_{l,j+1}^k+s_{l,j-1}^k-4s_{l,j}^k$

Step 3: fix  $r, \vec{p}, s, \vec{n}, \vec{m}, \vec{w}$  to solve  $q$

$$\varepsilon_3(q)=\min\left\{E(q)=\alpha\int_{\Omega}|q|dx+\int_{\Omega}\sigma_3^k\left(q-\nabla\vec{n}\right)dx+\frac{\mu_3}{2}\int_{\Omega}\left(q-\nabla\vec{n}\right)^2dx\right\} \quad (18)$$

Based on the generalized soft threshold formulation (GSTF), Eq. (18) can be solved as

$$q^{k+1}=\max\left(\left|\nabla\vec{n}^k-\frac{\sigma_3^k}{\mu_3}\right|-\frac{\alpha}{\mu_3},0\right)\frac{\nabla\vec{n}^k-\frac{\sigma_3^k}{\mu_3}}{\left|\nabla\vec{n}^k-\frac{\sigma_3^k}{\mu_3}\right|},0\frac{\vec{0}}{|\vec{0}|}=0 \quad (19)$$

Step 4: fix  $r, s, q, \vec{n}, \vec{m}, \vec{w}$  to solve  $\vec{p}$

$$\varepsilon_4(\vec{p})=\min\left\{E(\vec{p})=\int_{\Omega}\sigma_1^k\left(|\vec{p}|-|\vec{p}\cdot\vec{m}|\right)dx+\frac{\mu_1}{2}\int_{\Omega}\left(|\vec{p}|-|\vec{p}\cdot\vec{m}|\right)dx\right. \\ \left.+\int_{\Omega}\vec{\sigma}_2^k\left(\vec{p}-\nabla r\right)dx+\frac{\mu_2}{2}\int_{\Omega}\left(\vec{p}-\nabla r\right)^2dx\right\} \quad (20)$$

Its GSTF is

$$\vec{p}_i^{k+1}=\max\left(\left|\nabla r-\frac{\vec{\sigma}_2^k}{\mu_2}+\frac{(\sigma_1^k+\mu_1)\vec{m}^k}{\mu_2}\right|-\frac{\sigma_1^k+\mu_1}{\mu_2},0\right)\frac{\nabla r-\frac{\vec{\sigma}_2^k}{\mu_2}+\frac{(\sigma_1^k+\mu_1)\vec{m}^k}{\mu_2}}{\left|\nabla r-\frac{\vec{\sigma}_2^k}{\mu_2}+\frac{(\sigma_1^k+\mu_1)\vec{m}^k}{\mu_2}\right|},0\frac{\vec{0}}{|\vec{0}|}=0 \quad (21)$$

Step 5: fix  $r, s, q, \vec{p}, \vec{m}, \vec{w}$  to solve  $\vec{n}$

$$\varepsilon_5(\vec{n})=\min\left\{E(\vec{n})=\int_{\Omega}\sigma_3^k\left(q-\nabla\vec{n}\right)dx+\frac{\mu_3}{2}\int_{\Omega}\left(q-\nabla\vec{n}\right)^2dx\right. \\ \left.+\int_{\Omega}\vec{\sigma}_4^k\left(\vec{n}-\vec{m}\right)dx+\frac{\mu_4}{2}\int_{\Omega}\left(\vec{n}-\vec{m}\right)^2dx\right\} \quad (22)$$

Its E-L equation is

$$\nabla\sigma_3+\mu_3\nabla\left(q-\nabla\vec{n}\right)+\vec{\sigma}_4+\mu_4\left(\vec{n}-\vec{m}\right)=0 \quad (23)$$

Given that

$$\begin{cases} N1 = \mu_3 \left( n1_{i+1,j}^k + n1_{i-1,j}^k + \frac{1}{4} \left( n2_{i+1,j+1}^k + n2_{i-1,j-1}^k - n2_{i+1,j-1}^k - n2_{i-1,j+1}^k \right) \right) \\ N2 = \mu_3 \left( n2_{i,j+1}^k + n2_{i,j-1}^k + \frac{1}{4} \left( n1_{i+1,j+1}^k + n1_{i-1,j-1}^k - n1_{i+1,j-1}^k - n1_{i-1,j+1}^k \right) \right) \end{cases} \quad (24)$$

The solution of  $\vec{n}$  is

$$\begin{cases} \vec{n}1^{k+1} = \frac{\left( N1 + \mu_4 \left( \vec{m}_1 \right) - \vec{\sigma}_{41} - \frac{\partial \sigma_3}{\partial x} - \mu_3 \left( \frac{\partial q}{\partial x} \right) \right)}{(2\mu_3 + \mu_4)} \\ \vec{n}2^{k+1} = \frac{\left( N2 + \mu_4 \left( \vec{m}_2 \right) - \vec{\sigma}_{42} - \frac{\partial \sigma_3}{\partial y} - \mu_3 \left( \frac{\partial q}{\partial y} \right) \right)}{(2\mu_3 + \mu_4)} \end{cases} \quad (25)$$

Step 6: fix  $r, s, q, \vec{p}, \vec{n}, \vec{w}$  to solve  $\vec{m}$

$$\varepsilon_6(\vec{m}) = \min \left\{ E(\vec{m}) = \int_{\Omega} \sigma_1^k \left( |\vec{p}| - \vec{p} \cdot \vec{m} \right) dx + \frac{\mu_1}{2} \int_{\Omega} \left( |\vec{p}| - \vec{p} \cdot \vec{m} \right) dx \right. \\ \left. + \int_{\Omega} \vec{\sigma}_4^k \left( \vec{n} - \vec{m} \right) dx + \frac{\mu_4}{2} \int_{\Omega} \left( \vec{n} - \vec{m} \right)^2 dx \right\} \quad (26)$$

Its E-L equation is

$$\vec{m}^{k+1} = \frac{\vec{\sigma}_1^k \vec{p}^k + \frac{1}{2} \left( \mu_1 \vec{p}^k \right)}{\mu_4} + \vec{n}^k \quad (27)$$

In order to meet the constraint  $|\vec{m}| \leq 1$ , the following projection formation is imposed on  $\vec{m}$ :

$$\vec{m}^{k+1} = \frac{\vec{m}^k}{\max \left( |\vec{m}^k|, 1 \right)} \quad (28)$$

Step 7: fix  $r, s, q, \vec{p}, \vec{m}, \vec{n}$  and solve  $\vec{w}$ :

$$\varepsilon_7(\vec{w}) = \min \left\{ E(\vec{w}) = \beta \int_{\Omega} |\vec{w}| dx + \int_{\Omega} \vec{\sigma}_5^k \left( \vec{w} - \nabla s \right) dx + \frac{\mu_5}{2} \int_{\Omega} \left( \vec{w} - \nabla s \right)^2 dx \right\} \quad (29)$$

Its GSTF is

$$\vec{w}^{k+1} = \max \left( \left| \nabla s^k - \frac{\vec{\sigma}_5^k}{\mu_5} \right| - \frac{\beta}{\mu_5}, 0 \right) \frac{\nabla s^k - \frac{\vec{\sigma}_5^k}{\mu_5}}{\left| \nabla s^k - \frac{\vec{\sigma}_5^k}{\mu_5} \right|}, 0 \frac{\vec{0}}{|\vec{0}|} = 0 \quad (30)$$



Step 8: update the Lagrange multipliers

$$\begin{cases} \sigma_1^{k+1} = \sigma_1^k + \mu_1 \left( |\vec{p}^k - \vec{p}^k \cdot \vec{m}^k| \right) \\ \vec{\sigma}_2^{k+1} = \vec{\sigma}_2^k + \mu_2 \left( \vec{p}^k - \nabla r^k \right) \\ \sigma_3^{k+1} = \sigma_3^k + \mu_3 \left( q^k - \nabla \vec{n}^k \right) \\ \vec{\sigma}_4^{k+1} = \vec{\sigma}_4^k + \mu_4 \left( \vec{n}^k - \vec{m}^k \right) \\ \vec{\sigma}_5^{k+1} = \vec{\sigma}_5^k + \mu_5 \left( \vec{w}^k - \nabla s^k \right) \end{cases} \quad (31)$$

For clarity, the overall algorithm framework for solving the proposed variational model is summarized as follows.

**Algorithm 1** The computational procedure of the proposed method.

---

**Algorithm 1** The computational procedure of the proposed method

---

1. Input: Degraded underwater image
  2. Output: Restored underwater image
  3. Using dark channel prior and red channel prior to estimate the global background light and transmission map via (2)-(6)
  4. Initialization: set  $r, s, q, \vec{p}, \vec{m}, \vec{n}, \vec{w}, \sigma_1, \vec{\sigma}_2, \sigma_3, \vec{\sigma}_4, \vec{\sigma}_5$  as zeros,  $r_0 = \log\left(\frac{1}{t_0}\right)$ ,  
parameters:  $\alpha=7, \beta=2, \mu=0.35, \mu_1=0.0001, \mu_2=1, \mu_3=1000, \mu_4=0.01, \mu_5=0.2$ .
  5. Solve the following sub-problems alternatively
    - (i) fix  $s, q, \vec{p}, \vec{m}, \vec{n}, \vec{w}$  to solve  $r$  via (12)
    - (ii) fix  $r, q, \vec{p}, \vec{m}, \vec{n}, \vec{w}$  to solve  $s$  via (15)
    - (iii) fix  $r, s, \vec{p}, \vec{m}, \vec{n}, \vec{w}$  to solve  $q$  via (18)
    - (iv) fix  $r, s, q, \vec{m}, \vec{n}, \vec{w}$  to solve  $\vec{p}$  via (20)
    - (v) fix  $r, s, q, \vec{p}, \vec{m}, \vec{w}$  to solve  $\vec{n}$  via (22)
    - (vi) fix  $r, s, q, \vec{p}, \vec{n}, \vec{w}$  to solve  $\vec{m}$  via (26)
    - (vii) fix  $r, s, q, \vec{p}, \vec{m}, \vec{n}$  to solve  $\vec{w}$  via (29)
  6. Update the Lagrange multipliers via (31)
  7. Return the recovered image  $J$
  8. End
-

## 4 Experimental results and discussion

In this section, comparison experiments conducted on real underwater images and the analysis of the influence of experimental parameters are carried out, respectively. In the qualitative and quantitative comparisons, the state-of-the-art methods used for comparison include contrast limited adaptive histogram equalization (CLAHE), multi-scale Retinex with color restoration (MSRCR), dark channel prior (DCP) [16], wavelength compensation and image dehazing (WCID) [4], and automatic red-channel (ARC) [11], multi-scale correlated wavelet (MSCW) [27], Kimmel's variational framework for Retinex [23]. All the experiments are implemented in MATAB R2016b on an Intel 2.8GHz PC with 4GB RAM.

### 4.1 Qualitative assessment

First, we present the recovered results compared with the original ones to demonstrate the performance of the proposed method, as shown in Fig. 1. Figure 1 (a) shows three underwater degraded images suffer from low contrast, haze and noise. Figure 1 (b) and (c) present the result of proposed method and the corresponding energy curve verse number of iterations. It can be seen that our proposed algorithm achieves a good visual outcome in removing haze, suppress noise and improving contrast. Moreover, its high-efficiency in convergence with fewer iterations is illustrated in Fig. 1 (c). In addition, to evaluate the computational efficient of the proposed method, we set the times of iterations to 5, 10, 20 to restore different size of Fig. 1(a)–1(c). Their calculated runtimes with different iterations are shown in Table 1. It can be

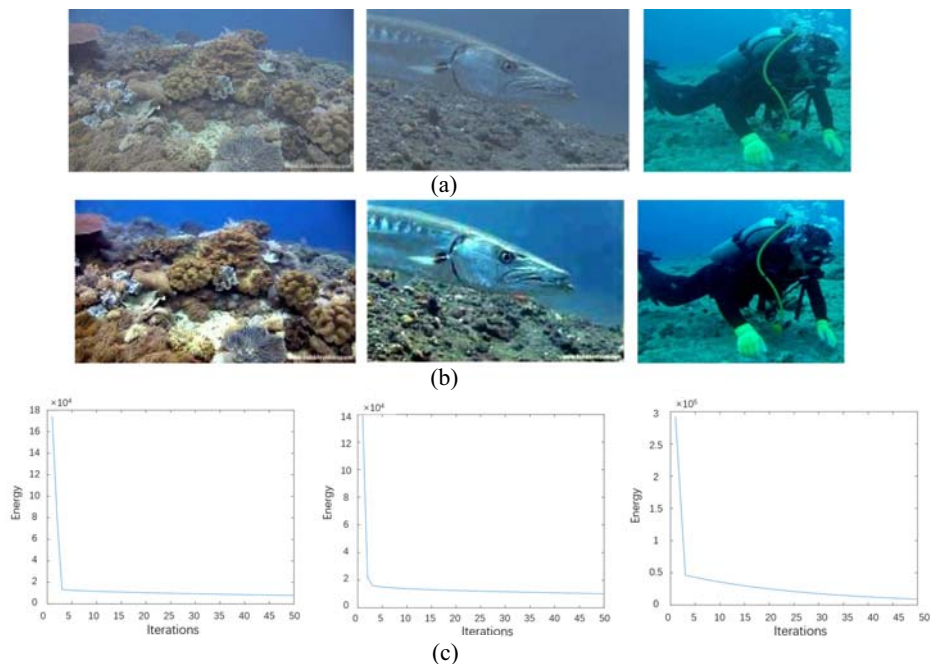


**Fig. 1** Real underwater image tests. (a) raw underwater image, (b) the corresponding recovered results, (c) the energy convergence curve

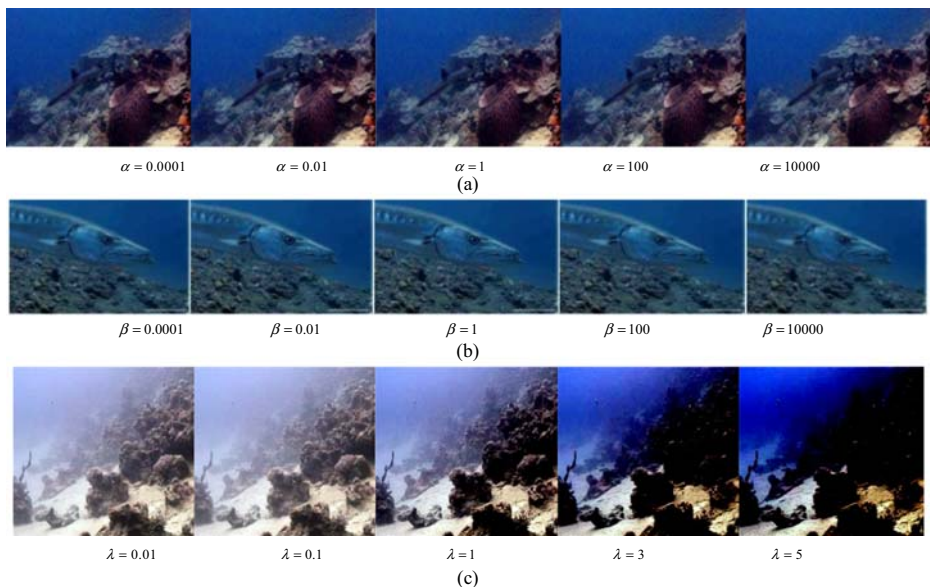
**Table 1** Runtime of proposed method

Image	5 iterations	10 iterations iterations	20 iterations
Figure 1(a-1)	0.8297	1.1062	1.1062
Figure 1(a-2)	0.8205	1.0440	1.4292
Figure 1(a-3)	2.3929	3.5905	6.5489

concluded that the cost of one iteration of the proposed method is around 0.1 s to 0.3 s, which achieves acceptable outcomes of computational efficiency using the fast ADMM algorithm.

As shown in Eq. (10), the proposed energy functional contains three parameters including  $\alpha$ ,  $\beta$ , and  $\lambda$ . As mentioned before, all of them are free positive parameters to weight the three corresponding terms. In this section, we will analyze the influence of these three parameters. Figure 2 shows the results with different values of parameters  $\alpha$ ,  $\beta$ , and  $\lambda$  after employing our dehazing and denoising method. In our experiment, we vary one by fixing another two parameters.

First, we set the constant values of  $\beta = 7$  and  $\lambda = 1$ , and change  $\alpha$  from  $10^{-4}$  to  $10^4$ . From Fig. 2 (a), we can see that some valuable information will be missing when  $\alpha$  is too small or too large, especially in the shaded areas. Figure 2 (b) displays the recovered results when we vary the values of  $\beta$ . Here, we fix  $\alpha = 7$ ,  $\lambda = 1$  and change  $\beta$  from  $10^{-4}$  to  $10^4$ . Visually, the results are basically similar no matter when  $\beta$  increases and  $\beta$  decreases. Thus, our algorithm is minimally affected by varying the parameter  $\beta$ . Next, we study the effect of  $\lambda$ . Figure 2 (c) presents the result with different  $\lambda$  by fixing  $\alpha = 7$  and  $\beta = 7$ . Obviously, the parameter  $\lambda$  determines the dehazing level. We can observe that the results have less haze and become darker when  $\lambda$  increases. It should be noted that a larger  $\lambda$  will produce a poorer outcome. In our test, we find that  $\lambda \in [0.8 - 1.5]$  could be more suitable.

**Fig. 2** The results with different  $\alpha$ ,  $\beta$ ,  $\lambda$  in (a), (b), (c), respectively

For comparison purposes, we choose six typically underwater images captured in different challenging conditions, such as hazy, fuzzy, color faded, nonuniform illumination, and noise, as shown in Fig. 3(a). Figure 3(b)-(h) lists the corresponding restored results after employ

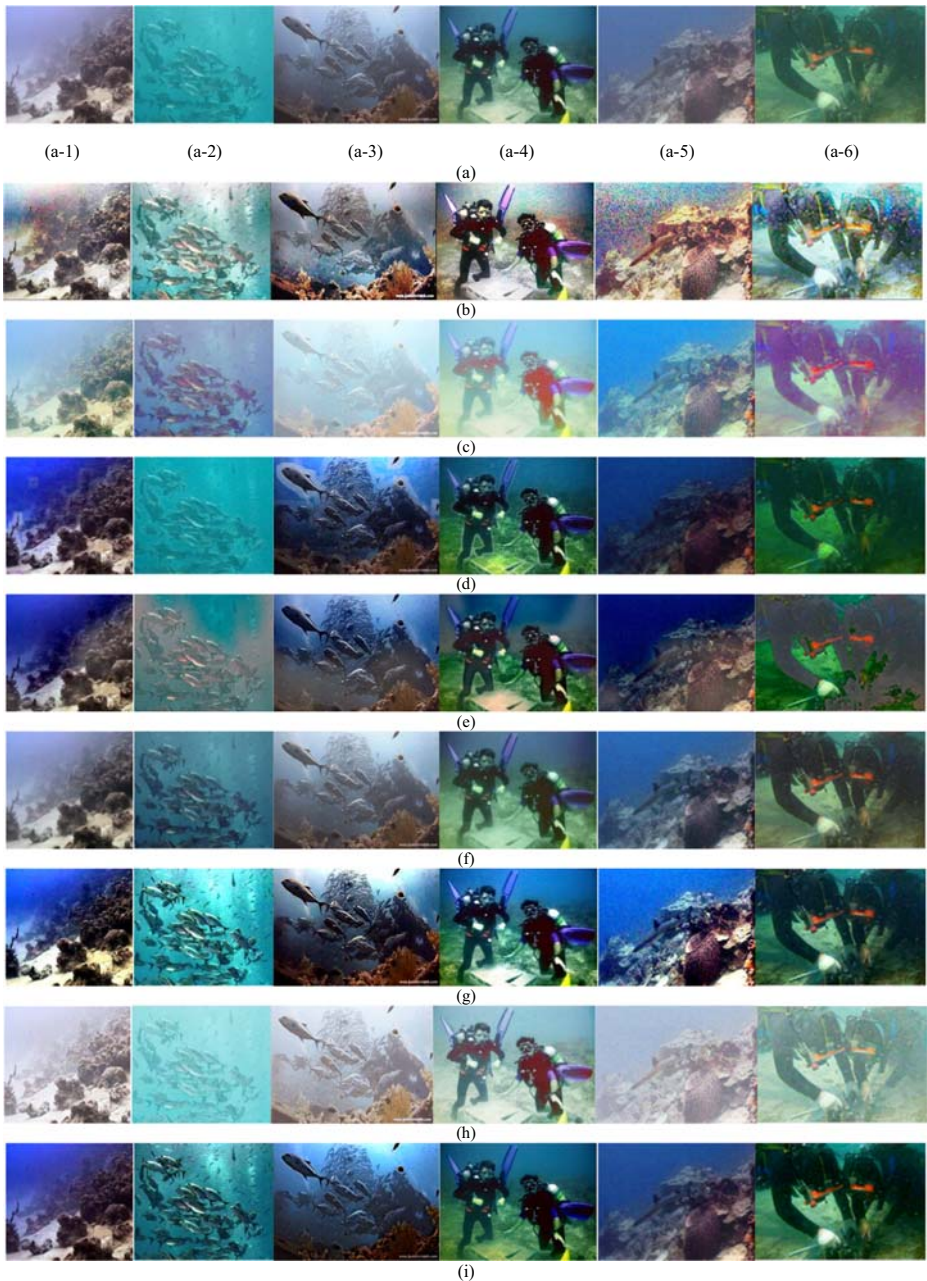


**Fig. 3** Qualitative comparison, (a) Original underwater image under different challenging scenes, the corresponding recovered results of (b) CLAHE method, (c) MSRCR method, (d) DCP method, (e) WCID method, (f) ARC method, (g) MSCW method, (h) Kimmel's, (i) the proposed method



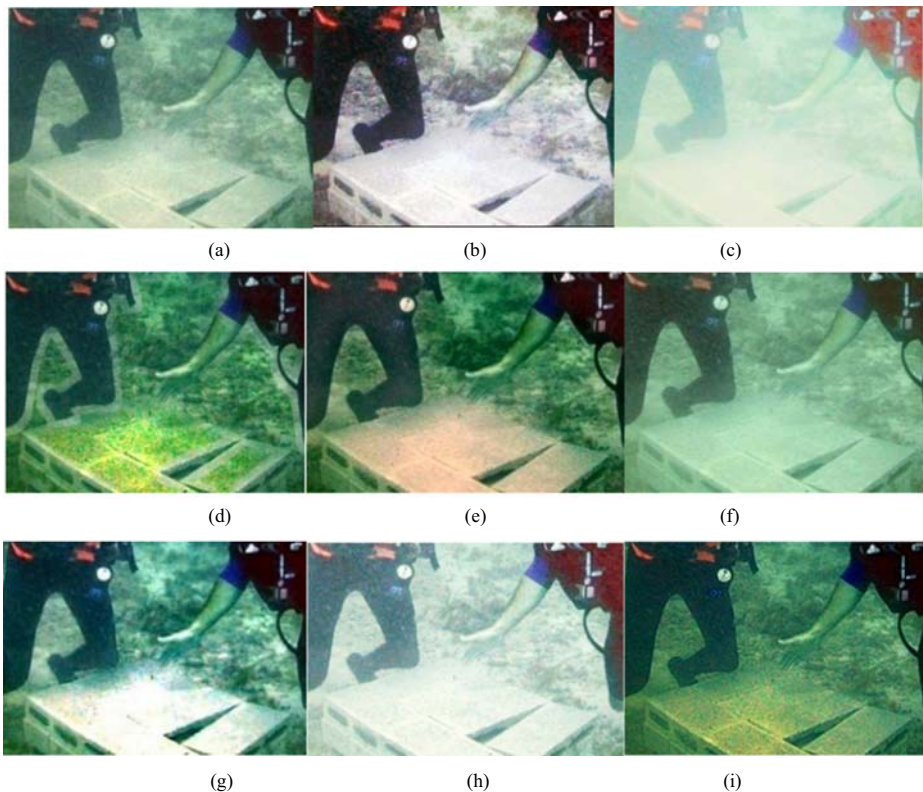


**Fig. 4** Zoomed small sub-regions for detail comparison, (a) the original sub-region, (b)–(i) the recovered results of the seven compared methods

CLAHE, MSRCR, DCP, WCID, ARC, MSCW, Kimmel's Variational Retinex and the proposed method, respectively. As we can observe from Fig. 3(b), CLAHE method achieves a good improvement in color correction and contrast enhancement. However, CLAHE algorithm also has a problem of over-amplifying the noise. As shown in Fig. 3(c), the MSRCR method can generate a high color saturation recovered image, but it may generate some overexposed regions in the foreground. Although the contrast and color saturation are enhanced by CLAHE and MSRCR methods, there is still room for improvement in details and

**Table 2** FADE value of different compared methods

Method	Figure 3(a-1)	Figure 3(a-2)	Figure 3(a-3)	Figure 3(a-4)	Figure 3(a-5)	Figure 3(a-6)	Average
Original	0.8282	0.5016	0.6469	0.4729	0.6564	0.7789	0.6474
CLAHE	0.3619	0.3938	0.2606	0.3574	0.2439	0.2676	0.3142
MSRCR	0.9265	0.7971	1.8929	1.3063	0.3656	0.5536	0.9737
DCP	0.2214	0.2747	0.1938	<b>0.1615</b>	0.3343	0.2821	0.2446
WCID	0.2730	0.6429	0.2872	0.2950	0.2568	0.3950	0.3583
ARC	0.5977	0.3636	0.6384	0.3696	0.2812	0.4567	0.4512
MSCW	0.2008	0.2525	0.2957	0.2787	0.2188	0.3729	0.2699
Kimmel's	1.0154	0.7909	0.8490	0.7772	0.3452	0.6834	0.7435
Proposed	<b>0.1992</b>	<b>0.2485</b>	<b>0.1429</b>	0.2129	<b>0.1241</b>	<b>0.2055</b>	<b>0.1889</b>

**Table 3** CQE value of different compared methods

Method	Figure 3(a-1)	Figure 3(a-2)	Figure 3(a-3)	Figure 3(a-4)	Figure 3(a-5)	Figure 3(a-6)	Average
CLAHE	1.0014	<b>1.0043</b>	<b>1.2362</b>	0.9062	1.1041	0.7789	1.0051
MSRCR	1.0962	0.8837	0.9188	0.8400	1.0853	1.0023	0.9910
DCP	1.1344	0.6309	1.1204	0.9096	1.0731	0.8439	0.9520
WCID	1.0591	0.8629	1.1066	0.8374	1.0058	0.9366	0.9680
ARC	1.0120	0.6968	0.9553	0.7236	1.0117	0.9336	0.8889
MSCW	1.1018	0.9319	1.0787	<b>0.9152</b>	1.1717	0.9436	1.0238
Kimmel's	1.0277	0.8921	1.0542	0.7535	0.9959	0.9598	0.9472
Proposed	<b>1.1482</b>	0.9035	1.0957	0.8657	<b>1.2009</b>	<b>1.0160</b>	<b>1.0383</b>

visibility due to these methods without considering the underwater optical image formation model (i.e. the details of the men's hand and head in the results obtained from Fig. 3(a-6) are blurred). From Fig. 3(d) and 3(e), it can be seen that DCP and WCID methods can effectively remove haze because both the algorithms are designed based on image formation model. Nevertheless, the backgrounds of some restored images are too dark owing to inaccurate estimation of background light and they also almost have no effect on improving contrast and reducing noise. Besides, in some cases, WCID method may bring color distortion. Similarly, the recovered results in Fig. 3(f) shows that the ARC method has a poor performance on removing haze. The MSCW method successes in dehazing and enhancing contrast, but the exposure operation may lead to a non-uniform illumination, as show in Fig. 3(g). As shown in Fig. 3(h), in most cases, Kimmel's method produces unsatisfied results and brings considerable artifacts and noise. Although the variational Retinex method has a good performance on low-light scene. However, they often saturate pixels without taking into account the underwater image information model, leading to no estimation of the underwater background light  $B$  and underwater medium transmission map  $t$ . Hence, it is not suitable for directly application to underwater image restoration. Fortunately, in Fig. 3(i), we can observe that the proposed method achieves a better visual result, especially in dehazing and denoising.

To further see the detailed superiority of the proposed method, we crop a rectangle area from the image of Fig. 3(a-4). The corresponding zoomed small sub-regions are displayed in Fig. 4. From Fig. 4(b)-(h), the seven methods used for comparison have similar problems in preserving texture features and eliminating non-uniform illumination. In contrast, it can be observed that the edge and valuable information in box are well preserved after using our proposed method from Fig. 4(i).

**Table 4** NSS value of different compared methods

Method	Figure 3(a-1)	Figure 3(a-2)	Figure 3(a-3)	Figure 3(a-4)	Figure 3(a-5)	Figure 3(a-6)	Average
CLAHE	3.2329	2.5643	3.3702	2.8281	<b>2.5359</b>	2.6712	2.8671
MSRCR	2.9149	2.4961	2.5193	2.4472	2.3838	2.7171	2.5797
DCP	3.3727	2.0763	3.3944	3.0171	2.1854	2.0988	2.6907
WCID	3.1686	2.1595	3.1830	<b>3.0664</b>	2.4569	2.0796	2.6856
ARC	3.2426	2.5510	3.1470	3.0548	2.3786	2.4294	2.8005
MSCW	3.1127	2.4865	3.4911	3.0564	2.3630	2.1656	2.7792
Kimmel's	3.3078	2.3249	3.1962	2.3713	2.4049	2.6806	2.7142
Proposed	<b>3.4756</b>	<b>2.6541</b>	<b>3.4931</b>	2.7426	2.4132	<b>2.7326</b>	<b>2.9185</b>

**Table 5** UCIQE value of different compared methods

Method	Figure 3(a-1)	Figure 3(a-2)	Figure 3(a-3)	Figure 3(a-4)	Figure 3(a-5)	Figure 3(a-6)	Average
CLAHE	0.5453	0.4943	0.5839	0.6099	0.5680	0.5570	0.5597
MSRCR	0.5102	0.4195	0.4653	0.4078	0.5220	0.4701	0.4658
DCP	0.5980	0.3475	0.6160	0.6319	0.5932	0.4747	0.5435
WCID	0.5999	0.4388	0.5964	0.6269	0.5705	0.4877	0.5533
ARC	0.5533	0.4484	0.5428	0.5561	0.5583	0.4989	0.5263
MSCW	0.6014	0.4936	<b>0.6241</b>	0.6104	<b>0.6493</b>	0.5508	0.5882
Kimmel's	0.4501	0.3114	0.4594	0.5061	0.3999	0.3948	0.4202
Proposed	<b>0.6154</b>	<b>0.5350</b>	0.6016	<b>0.6493</b>	0.6351	<b>0.5745</b>	<b>0.6020</b>

## 4.2 Quantitative assessment

To objectively evaluate the superiority of our proposed method, four non-reference metrics namely fog aware density evaluator (FADE) [5], colour quality enhancement (CQE) [31], natural scene statistics (NSS) [9] and the underwater color image quality evaluation metric (UCIQE) [46] are used for quantitative comparison. The FADE metric is used frequently to predict perceptual fog density, which correlates well with the viewpoint of subjective human perception. The indicator CQE is a simple combination of colorfulness, sharpness and contrast in RGB color space. The UCIQE metric is similar to the CQE metric but differs in the combination of chroma, saturation, and contrast in CIE Lab color space. The NSS metric is often used for assessment of contrast-distorted images.

The calculated results of these metrics on the recovered image in Fig. 3 are illustrated in Tables 2, 3, 4, and 5, respectively. The best outcomes are highlighted in bold format in these tables. From Tables 2, 3, 4, and 5, it can be seen that our dehazing and denoising method outperforms the other seven methods in terms of FADE CQE, NSS, and UCIQE values. The highest FADE values of the proposed methods verify its superiority in defogging, as shown in Table 2. For CQE in Table 3, we can observe that our proposed method achieves highest average value with 1.0383, followed by MSCW method. The average values obtained from MSRCR, DCP, ARC, WCID and Kimmel's are all less than 1.0. Similarly, as shown in Table 4, the higher NSS score of the proposed method also demonstrate that our method can effectively enhance contrast and reveal more details. In Table 5, we can see that the average UCIQE scores of the seven compared methods are all below 0.6. Badly, Kimmel's method achieves the lowest value with 0.4202. In contrast, in most cases, the UCIQE values of ours' are more than 0.6. The best UCIQE value indicates that the recovered underwater images of our proposed method have a good balance in chroma, saturation, and contrast.

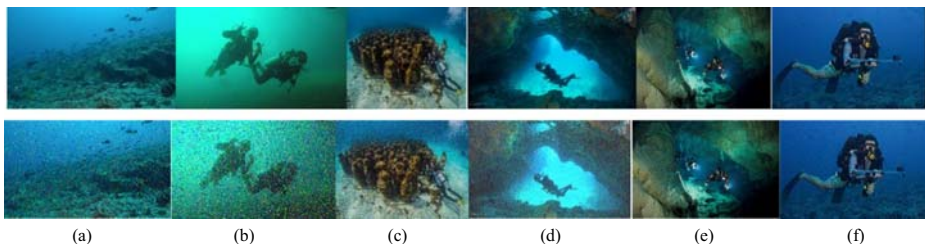


**Fig. 5** Six real underwater images added with various noise, (a-b) salt & pepper noise added, (c-d) Gaussian noise added, (e-f) Poisson noise added

**Table 6** PSNR value of different compared methods

Method	Figure 5(a)	Figure 5(b)	Figure 5(c)	Figure 5(d)	Figure 5(e)	Figure 5(f)
Original	40.0911	34.3112	26.8056	24.3488	34.2926	33.7543
CLAHE	26.3053	26.8334	25.2961	24.9400	24.4626	25.2108
MSRCR	24.7003	25.4072	24.2485	24.2559	24.4486	24.1385
DCP	27.0911	30.3112	28.1907	24.8759	36.6157	34.4946
WCID	31.0076	29.8850	28.6094	25.4936	33.4301	33.2420
ARC	30.4561	29.7644	30.0145	24.7502	32.5646	31.3281
MSCW	28.9682	32.2766	27.2293	26.4503	29.8149	28.7515
Kimmel's	34.3421	32.2154	31.1421	26.3412	35.4537	31.8990
Proposed	<b>36.7282</b>	<b>33.6628</b>	<b>36.2701</b>	<b>27.4639</b>	<b>41.0435</b>	<b>37.2231</b>

For further assessment of the denoising effect, variations of noise (i.e. salt & pepper noise with 0.2, Gaussian noise with 0.05, and Poisson noise) are further added to six real underwater images, as shown in Fig. 5. The ratio indicator PSNR is employed for the performance evaluation, the comparisons of PSNR values using different models are presented in Table 6. It should be noted that higher PSNR values mean better results. As shown in the first two columns of Table 6, for salt & pepper noise, all the obtained PSNR values after employing these compared algorithms are lower than their original values. However, our denoising method still get the highest score among them. For Gaussian noise, the lower PSNR values of CLAHE and MSRCR indicate that noise is amplified. For Poisson noise, only DCP and our method can effectively reduce it. Overall, we can conclude that our proposed method stands out among these compared methods in suppressing noise, especially for Gaussian and Poisson noise.

## 5 Conclusion

A novel variational approach incorporating curvature regularization and underwater image formation is proposed in this paper, which aims to tackle problems of underwater image dehazing and denoising. The three prominent aspects of our variational framework lie in: (1) the dark channel prior and underwater red channel prior are used as a guidance to provide information of the underwater global background light and the underwater transmission map; (2) Integration with variational model using high-order curvature term and total variation term as regularizers, a significant accuracy increase is achieved reflected in the evaluation section; (3) The ADMM algorithm is designed into the calculation procedure for the non-smooth optimization problem, which can also guarantee the convergence and efficiency. Extensive experiments demonstrate that the proposed method not only achieves satisfactory haze-free results, but also possesses capabilities of color balancing and contrast enhancing, especially produces excellent details and edge preservation results. It can be easily observed that all these advantages stand out more through the qualitative and quantitative comparisons with the other seven algorithms.

**Acknowledgements** The research work is partially supported by National Natural Science Foundation of China (No. 61901240), China Scholarship Council (No. 201908370002), the Natural Science Foundation of Shandong Province, China (No. ZR2019BF042), and the China Postdoctoral Science Foundation (No. 2017M612204). The first author would like to thank Lu Tan for doing many researches about variational method based on image



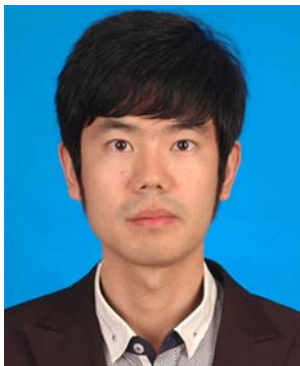
analysis, also thank Xiangjun Du, Yi Zhao, and Xiaopeng Wang, who work in the experimental teaching centre for providing us with the experimental platform.

## References

1. Ancuti CO, Ancuti C, Vleeschouwer CD, Bekaert P (2017) Color balance and fusion for underwater image enhancement. *IEEE Trans Image Process* 27(1):379–393
2. Carlevaris-Bianco N, Mohan A, Eustice RM (2010) Initial results in underwater single image dehazing. *OCEANS 2010. MTS/IEEE SEATTLE*, Seattle, WA, pp. 1–8
3. Chang H, Lou Y, Duan Y, Marchesini S (2018) Total variation-based phase retrieval for Poisson noise removal. *SIAM J Imaging Sci* 11(1):24–55
4. Chiang J, Chen Y (2012) Underwater image enhancement by wavelength compensation and dehazing. *IEEE Trans Image Process* 21(4):1756–1769
5. Choi LK, You J, Bovik AC (2015) Referenceless prediction of perceptual fog density and perceptual image defogging. *IEEE Trans Image Process* 24(11):3888–3901
6. Duan J, Pan Z, Zhang B, Liu W, Tai X (2015) Fast algorithm for color texture image inpainting using the non-local CTV model. *J Glob Optim* 62(4):853–876
7. Duan J, Tench C, Gottlob I, Proudlock F, Bai L (2017) Automated segmentation of retinal layers from optical coherent tomography images using geodesic distance. *Pattern Recogn* 72:158–175
8. Fang F, Fang L, Zeng T (2014) Single image dehazing and denoising: a fast variational approach. *SIAM J Imaging Sci* 7(2):969–996
9. Fang Y, Ma K, Wang Z, Lin W, Fang Z, Zhai G (2015) No-reference quality assessment of contrast-distorted images based on natural scene statistics. *IEEE Signal Process Lett* 22(7):838–842
10. Fu X, Liao Y, Zeng D, Huang Y, Zhang X, Ding X (2015) A probabilistic method for image enhancement with simultaneous illumination and reflectance estimation. *IEEE Trans Image Process* 24(12):4965–4977
11. Galdran A, Pardo D, Picón A, Alvarez-Gila A (2015) Automatic red-channel underwater image restoration. *J Vis Commun Image Represent* 26:132–145
12. Galdran A, Vazquezcorral J, Pardo D, Bertalmio M (2017) Fusion-based variational image dehazing. *IEEE Signal Process Lett* 24(2):151–155
13. Gordon HR (1989) Can the lambert-beer law be applied to the diffuse attenuation coefficient of ocean water? *Limnol Oceanogr* 34(8):1389–1409
14. Gould RW, Arnone RA, Martinolich PM (1999) Spectral dependence of the scattering coefficient in case 1 and case 2 waters. *Appl Opt* 38(12):2377–2383
15. Guo Q, Xue L, Tang R, Guo L (2017) Underwater image enhancement based on the dark channel prior and attenuation compensation. *J Ocean Univ China* 16(5):757–765
16. He K, Jian S, Tang X (2011) Single image haze removal using dark channel prior. *IEEE Trans Pattern Anal Mach Intell* 33(12):2341–2353
17. Hou G, Pan Z, Huang B, Wang G, Luan X (2018) Hue preserving-based approach for underwater colour image enhancement. *IET Image Process* 12(2):292–298
18. Hou G, Pan H, Huang B, Wang G, Wei W, Pan Z (2018) Efficient L-1-based nonlocal total variational model of Retinex for image restoration. *J Electron Imaging* 27(5):051207
19. Hou G, Pan Z, Wang G, Yang H, Duan J (2019) An efficient nonlocal variational method with application to underwater image restoration. *Neurocomputing* 369:106–121
20. Hou G, Li J, Wang G et al (2020) A novel Dark Channel prior guided Variational framework for underwater image restoration. *J Vis Commun Image Represent* 66:102732
21. Jaffe JS (1990) Computer modeling and the design of optimal underwater imaging systems. *IEEE J Ocean Eng* 15(2):101–111
22. Kim JH, Jang W, Sim JY, Kim CS (2013) Optimized contrast enhancement for real-time image and video dehazing. *J Vis Commun Image Represent* 24(3):410–425
23. Kimmel R, Elad M, Shaked D, Keshet R, Sobel I (2003) A variational framework for retinex. *Int J Comput Vis* 52(1):7–23
24. Kumar N, Sardana HK, Shome SN (2018) Saliency based shape extraction of objects in unconstrained underwater environment. *Multimedia tools and applications* 1–19
25. Li C, Guo J, Cong R, Pang Y, Wang B (2016) Underwater image enhancement by dehazing with minimum information loss and histogram distribution prior. *IEEE Trans Image Process* 25(12):5664–5677
26. Li X, Yang Z, Shang M, Hao J (2016) Underwater image enhancement via dark channel prior and luminance adjustment. *OCEANS 2016 - Shanghai*, pp. 1–5.
27. Liu X, Zhang H, Cheung Y, You X, Tang Y (2017) Efficient single image dehazing and denoising: an efficient multi-scale correlated wavelet approach. *Comput Vis Image Underst* 162:23–33

28. Lu J, Wang G, Pan Z (2017) Nonlocal active contour model for texture segmentation. *Multimed Tools Appl* 76(8):10991–11001
29. Marques TP, Albu AB, Hoeberechts M (2018) Enhancement of low-lighting underwater images using dark channel prior and fast guided filters. *International conference on pattern recognition*. Springer, Cham
30. Mcglamery BL (1979) A computer model for underwater camera systems. *Proceedings of the SPIE* 208: 221–231
31. Panetta K, Gao C, Agaian S (2013) No reference color image contrast and quality measures. *IEEE Trans Consum Electron* 59(3):643–651
32. Peng Y, Cosman PC (2017) Underwater image restoration based on image blurriness and light absorption. *IEEE Trans Image Process* 26(4):1579–1594
33. Rizzini DL, Kallasi F, Oleari F, Caselli S (2015) Investigation of vision-based underwater object detection with multiple datasets. *Int J Adv Robot Syst* 12(6)
34. Rudin LI, Osher S, Fatemi E (1992) Nonlinear total variation based noise removal algorithms. *Physica D* 60(1–4):259–268
35. Schechner YY, Karpel N (2005) Recovery of underwater visibility and structure by polarization analysis. *IEEE J Ocean Eng* 30(3):570–587
36. Shu Q, Wu C, Zhong Q, Liu R (2018) Total generalized variation-regularized variational model for single image dehazing. In: 9th international conference on graphic and image processing (ICGIP 2017), 10615, 106152M
37. Surya Prasath VB, Kalavathi P (2016) Mixed noise removal using hybrid fourth order mean curvature motion. *Advances in Signal Processing and Intelligent Recognition Systems* 425:625–632
38. Tan L, Liu W, Pan Z (2018) Color image restoration and Inpainting via Multi-Channel Total curvature. *Appl Math Model* 61:280–299
39. Tan L, Pan Z, Liu W (2018) Image segmentation with depth information via simplified Variational level set formulation. *J Math Imaging Vis* 60(1):1–17
40. Tikhonov AN (1963) Regularization of incorrectly posed problems. *Soviet Math Dokl* 4(6):1624–1627
41. Wang G, Lu J, Pan Z, Miao Q (2017) Color texture segmentation based on active contour model with multichannel nonlocal and Tikhonov regularization. *Multimed Tools Appl* 76(22):24515–24526
42. Wang Z, Hou G, Pan Z et al (2018) Single image dehazing and denoising combining dark channel prior and variational models. *IET Comput Vis* 12(4):393–402
43. Wang G, Pan Z, Zhang Z (2019) Deep CNN Denoiser prior for multiplicative noise removal. *Multimed Tools Appl* 78(20):29007–29019
44. Wen H, Tian Y, Huang T, Gao W (2013) Single underwater image enhancement with a new optical model. 2013 IEEE international symposium on circuits and systems (ISCAS2013). IEEE.
45. Wu Q, Li Y, Lin Y (2017) The application of nonlocal total variation in image denoising for mobile transmission. *Multimed Tools Appl* 27(16):17179–17191
46. Yang M, Sowmya A (2015) An underwater color image quality evaluation metric. *IEEE Trans Image Process* 24(12):6062–6071
47. Zhang Y, Ben Hamza A (2007) Vertex-based diffusion for 3-D mesh Denoising. *IEEE Trans Image Process* 16(4):1036–1045
48. Zhang H, Yu J, Wang Z (2018) Probability contour guided depth map inpainting and superresolution using non-local total generalized variation. *Multimed Tools Appl* 77(7):9003–9020
49. Zhu W, Tai X, Tony C (2013) Augmented Lagrangian method for a mean curvature based image denoising model. *Inverse Problems & Imaging* 7(4):1409–1432

**Publisher's note** Springer Nature remains neutral with regard to jurisdictional claims in published maps and institutional affiliations.



**Guojia Hou** is an Assistant Professor at the College of Computer Science & Technology, Qingdao University. He received his BS degree in computer science in 2010 and his MS and PhD degrees in computer applications technology from the Ocean University of China in 2012 and 2015, respectively. He is the author of more than 20 journal and conference papers. His current research interests include image processing and pattern recognition.



**Jingming Li** received his B.Sc. degree from Nanjing University of Chinese Medicine. Now he is a master degree candidate in Qingdao University. His main research interest is image processing.



**Guodong Wang** is an Associate Professor at the College of Computer Science & Technology, Qingdao University. He received his MS degree in control theory and control engineering from Qingdao University of Science and Technology, and his PhD in pattern recognition and intelligent system from the Huazhong University of Science and Technology in 2008, respectively. His research interests include deep learning, face recognition, and intelligent video monitoring and analysis.



**Zhenkuan Pan** received his PhD in 1992 from the Shanghai Jiao Tong University of Science and Technology. Since 1996, he has been a Full Professor at Qingdao University. He is also a member of the virtual reality professional committee of China graphic image association. He is the author of more than 200 papers. His interests include computer vision, image processing, and pattern recognition. He is also working on the application of multibody system dynamics and control.



**Xin Zhao** received her B.Sc. degree from Taishan University. Now she is a master degree candidate in Qingdao University. Her main research interest is image processing.